# Morphological characterization of patterns in reaction-diffusion systems

K. R. Mecke*
*Center for Nonlinear Dynamics and Department of Physics, The University of Texas at Austin, Austin, Texas 78712*
(Received 24 October 1995)

Morphological measures for spatial patterns occuring as dissipative structures in systems driven far from equilibrium are introduced. They characterize the geometry and topology of the patterns and are capable to distinguish irregular structures with respect to the morphology. In particular, we analyze turbulent and regular patterns (Turing patterns) in chemical reaction-diffusion systems observed in a two-dimensional open gel reactor with a chlorite-iodide-malonic acid reaction. Introducing the concept of level contours, the measures turn out to be polynomials of low order (cubic and fourth degree) in the grey-scale level of the images. Thus the dependence on the experimental conditions is reflected only in a finite number of coefficients, which can be used as order parameters for the morphology of patterns. We observe a symmetry breaking of the polynomials when the type of the pattern changes from hexagons to turbulence or stripes. Therefore it is possible to describe the pattern transitions quantitatively and it may be possible to classify them in a similar way like thermodynamic phase transitions.

PACS number(s): 47.54.+r, 47.20.Hw, 05.70.Fh

## I. INTRODUCTION

Irregular spatial-temporal patterns occur in many systems, including chemical reaction-diffusion systems [1–6], Rayleigh-Benard convection [7,8] electrohydrodynamic convection [9], and surface waves [10,11]. The usual approaches to describe and characterize such complex spatial structures are, for instance, autocorrelation functions or Fourier transformations [1]. Whereas for regular patterns these measures provide useful information as, for example, about characteristic length scales and orientational order, they are incapable of distinguishing irregular structures of different topology.

Especially, they do not provide a description of the morphology of the patterns, i.e., of the content and shape of spatial structures. As an example, consider the three patterns shown in Fig. 1. The obvious difference between these patterns does not show up in their characteristic length scales but in the connectedness of white or black regions and in the bending or curvature of the stripes. Other features related to the content and shape of figures embedded in the patterns are, for instance, the white area or the length of the boundaries between black and white regions. Since photographs reveal such detailed spatial information and since the difference and the evolution of patterns are mostly recognized in the change of their shapes, it is important to define quantitative measures for such morphological characteristics. Moreover, the failure of quantities used in the analysis of low-dimensional chaotic systems, such as generalized dimensions and Lyapunov exponents, to describe spatial-temporal patterns demands measures quantifying the essential morphological features like the connectedness of spatial regions and the curvature of their boundaries.

Apart from singular patterns extended phase-diagrams of spatial structures were observed in the experiments mentioned above (see Fig. 10 in Ref. [1]). Unlike in equilibrium phase transitions the reproducible transition of one pattern type into another structure is not well understood. In recent theoretical studies [12,13] the occurrence of turbulence, i.e., the instability of regular stationary patterns, was related to the occurrence of topological defects, in analogy to phase transitions in two-dimensional statistical systems. Furthermore, quantitative measures of disorder in regular patterns were defined [14] and wavelet transforms are introduced to extract local amplitudes and phases of the pattern in order to analyze defects [15]. However, none of these approaches to analyze transitions of spatial patterns are focusing on their changes in morphology or shapes of connected regions, in particular, if many defects occur. The wavelet analysis of two-dimensional patterns is a difficult and nontrivial method which is often numerically inefficient. Therefore it is useful to look for a quantitative characterization of the morphology of spatial patterns which allows a direct and numerically robust way to analyze experimental data.

In this paper we introduce the Minkowski functionals as morphological measures for patterns. They are well-known in image analysis [16], mathematical morphology [17], and integral geometry [18]. A prominent member of this family of morphological measures is the Euler characteristic describing the topology, i.e., the connectivity of spatial patterns.

Although this approach is generally useful for dissipative structures in nonequilibrium systems, we study in this paper solely concentration patterns obtained in a chemical reaction, where the structures emerge out of the coupling of reaction dynamics and diffusion. The occurrence of stationary spatial patterns in chemical reaction-diffusion systems was already predicted by Turing [19] and was extensively investigated since then by theoretical and numerical studies [20]. The first experimental observation of stationary patterns in a gel reactor was in 1990 [3–5].

We consider Turing-type chemical spatial patterns in a two-dimensional open spatial reactor with a chlorite-iodide-malonic acid reaction. The experiments are described in detail in Ref. [1]. The patterns form in a thin, quasi-two-

*Permanent address: Bergische Universität Wuppertal, Fachbereich Physik, D-42097 Wuppertal, Federal Republic of Germany.

 

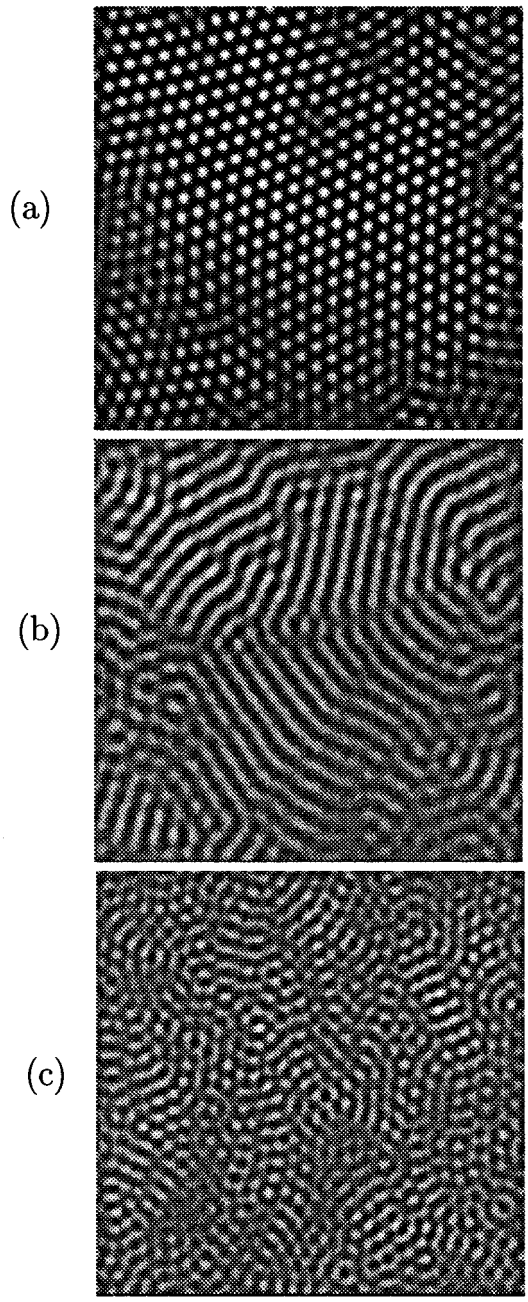


FIG. 1. Three types of chemical patterns were observed in Ref. [1], a hexagonal state (a), a lamellar stripe structure (b), and a turbulent pattern (c). The grey tones of the image correspond to the concentration of iodide $I_3^-$. Each images consists of a $512\times480$ array of pixels with 256 grey levels.

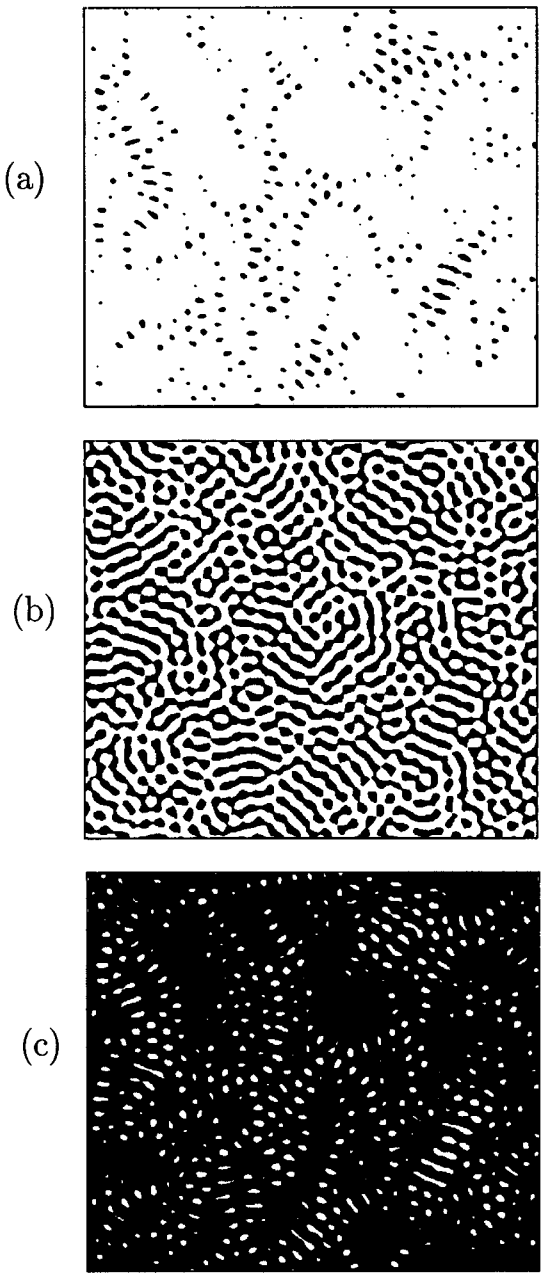


FIG. 2. Three black-and-white images derived from the turbulent pattern shown in Fig. 1(c) at three different grey levels $\rho=60$, 127, and 180. The image is white, where the grey level in Fig. 1(c) is higher than $\rho$. One can see clearly the different topologies of the images. At the threshold $\rho=127$ the black and white components are highly connected, whereas at $\rho=60$ ($\rho=180$) many disconnected black (white) components occur.

dimensional disk filled with polyacrylamide gel which prevents convection but allows for the diffusion of chemicals. Depending on the concentration of iodide $I_3^-$ the system changes in color from yellow to blue which is measured in digitized grey-scale images. Above critical values of the control parameters, i.e., temperature and reagent concentrations, spatial patterns spontaneously emerge from a spatially homogeneous system. Three different types of patterns are reported in Ref. [1], a hexagonal structure of isolated dots, a lamellar stripe structure broken up into domains of different orientations, and a structure of turbulent stripes, which change shape and orientation much faster than the usual moving of grain boundaries.

In the next section we introduce for these spatial patterns the concept of level contours and define the Minkowski functionals as morphological measures before we describe in the following section the results for the reported Turing patterns.

## II. LEVEL CONTOURS AND MINKOWSKI MEASURES

We show in Fig. 1 examples of the three different types of chemical patterns observed in Ref. [1], a hexagonal state (a),

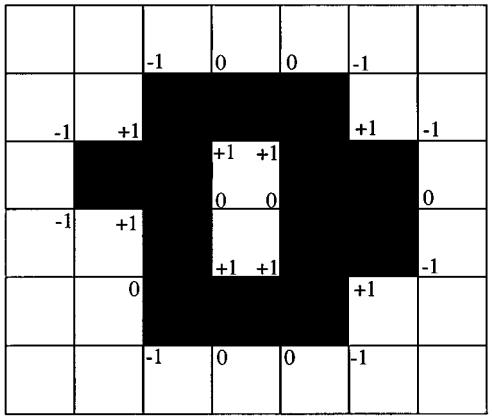


FIG. 3. A black-and-white digital image consists of a square lattice where each square has exactly four nearest and next-nearest neighbors. By counting the number of white squares one obtains for the area fraction $v=\frac{13}{42}$. The boundary length $s=\frac{4}{7}$ between the black and white regions is given by the number of sides joined by a black and white pixel. The number of connected black and white components in both cases one ($N_\rho^{(b)}=N_\rho^{(w)}=1$), since the surrounding white region does conventionally not count. The Euler characteristic is therefore zero ($\chi=0$), a result which can also be obtained by counting the local curvature variables located at the boundaries.

a lamellar stripe structure (b), and a turbulent pattern (c). The grey tones of the image correspond to the amount of the oxidized state in the system, i.e., inversely proportional to the concentration of iodide $I_3^-$. Each image consists of a $512\times480$ array of pixels with 256 grey levels.

In order to get detailed information about the spatial structure we want to look at the system at each grey level, i.e., we consider the so-called level contours. Thus we introduce a threshold variable $\rho=0,\ldots,255$ and reset the grey value at each pixel to either white or black depending on whether the original value is larger or lower than $\rho$, respectively. In this way we get 256 black-and-white images out of one grey-level image. In Fig. 2 we show three of them derived from the turbulent image shown in Fig. 1(c) at the levels $\rho=60$, 127, and 180. The qualitative features of the images varies drastically when the threshold parameter $\rho$ is changed.

Although the pictures in Fig. 2 are obviously descriptions of continuous patterns, i.e., describable by smooth boundary lines between black and white areas, they actually consist of a square lattice of pixels shown in Fig. 3. Thus each pixel has exactly four nearest neighbor pixels along the sides of the unit squares of the lattice and also four next-nearest neighbors connecting the diagonals of the unit squares. In order to avoid a somewhat arbitrary definition of continuous boundary lines on a large scale we want to introduce geometric measures right on the well-defined pixel level, which nevertheless describe the morphological differences of these discrete images in a continuous way. For this purpose we use Minkowski measures, well known in digital picture analysis [16] and integral geometry [17] for the characterization of black-and-white discrete images. Integral geometry generalizes curvature integrals over smooth surfaces to the case of surfaces with edges and corners. In the example of a two-dimensional digital picture such irregularities arise from the corners of the pixels, which make the Minkowski measures

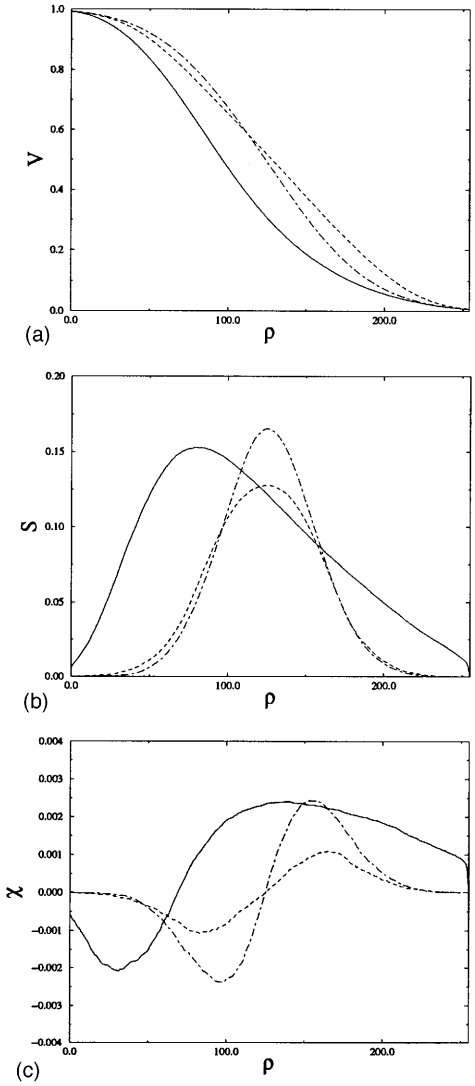


FIG. 4. The Minkowski measures, i.e. (a) the area fraction $v$, (b) the boundary length $s$, and (c) the Euler characteristic $\chi$, are shown for three typical patterns, a hexagonal state (full lines), a lamellar stripe structure (dashed), and a turbulent pattern (dash-dotted). (a) The area of the white region, i.e., the number of pixels with threshold larger than $\rho$, decreases monotonously from 1 to 0. In contrast to the stripe and turbulent pattern, which both show a nearly point-symmetric behavior with respect to $\rho=127$ and $v=0.5$, the hexagonal structure favors black areas. This can already be seen in the grey-scale image shown in Fig. 1(c). (b) The boundary length tends to zero for a nearly white ($\rho=0$) and black ($\rho=255$) image and reaches a maximum inbetween. Again the hexagonal pattern exhibits an asymmetry in $\rho$ with a maximum of the boundary length at smaller values of the threshold $\rho$ than for the stripe and turbulent structure with a maximum near $\rho=127$. (c) The Euler characteristic $\chi$ describes the topological structure of the pattern. It is negative (positive) if many disconnected black (white) components dominate the image. A vanishing Euler characteristic indicates a highly connected structure with equal amount of black and white components as it can be seen in Fig. 2.

the natural choice for the description of the geometry, or morphology, of digital pictures. These measures have already been applied in other physical systems where spatial patterns play an important role, e.g., for the description of micro-

emulsions [21,22], the large scale distribution of galaxies in the Universe [23], and percolation in porous media [24].

One obvious quantity describing the morphological differences of the images shown in Fig. 2 is the white area, i.e., the number of pixels $N_\rho$ with a grey level larger than $\rho$. Normalized by the total number of pixel $N$ the area fraction $v(\rho)=N_\rho/N$ decreases from 1 to 0 by increasing the threshold, which is shown in Fig. 4(a) for three typical patterns reported by Ref. [1], i.e., for a hexagonal state (full lines), a lamellar stripe structure (dashed), and a turbulent pattern (dashed-dotted).

Another morphological quantity shown in Fig. 4(b) is the length of the boundary line $s(\rho)=B_\rho/N$ between black and white regions measured as the number of pairs of neighbored black and white pixels $B_\rho$ normalized by the total number of pixels $N$. As expected, the boundary length $s$ starts at zero for the totally white image at $\rho=0$, increases, reaches a maximum value where the black and white areas are nearly equal, decreases, and finally ends at zero again for the complete black image at $\rho=255$.

The third quantity shown in Fig. 4(c) is the so-called Euler characteristic $\chi(\rho)=(N_\rho^{(w)}-N_\rho^{(b)})/N$, i.e., the difference of the number of black $N_\rho^{(b)}$ and white $N_\rho^{(w)}$ components normalized by $N$. A black or white component is defined as a region of connected black or white pixels, respectively. Thereby a black pixel is connected to another black one iff one can find a path of black pixels going in each step from one pixel to one of its four nearest neighbors. Due to the square-lattice structure of the pixels the definition for white components is slightly different. A white pixel is connected to another white one iff one can find a path of white pixels going in each step from one pixel to one of its four nearest neighbors or to one of its four next-nearest neighbors. Thus diagonal steps are allowed. We want to note that for the pictures considered here this difference plays no role, since always a path could be found avoiding diagonal steps.

In contrast to the surface area $v$ and the line length $s$ the Euler characteristic $\chi$ describes the pattern in a purely topological way, i.e., without refering to any kind of metric. It measures the connectivity of the black and white regions. Despite this global characterization of the pattern the Euler characteristic can be calculated in a local way. Consider, for example, one of the four corners of a black pixel and its three neighboring pixels joining at this corner as it is shown in Fig. 3. We design at each corner of a black pixel the values $-1$, 0, or $+1$ depending on the ''local curvature.'' According to Fig. 3 the curvature value is $-1$ iff both of the two nearest neighbors joining at the corner are white, it is $+1$ iff both of the two nearest neighbors joining at the corner are black and the third, next-nearest one is white, and it is 0 for all other cases. The sum of all these curvature values divided by $4N$ equals the Euler characteristic $\chi$. It can be shown that this definition of $\chi$ possesses a continuum limit for smooth boundaries, which is equal to the integral of the curvature along the boundary lines. Thus $\chi/s$ describes the mean curvature of the boundary between black and white domaines. As one can see in Fig. 2(a) at low thresholds many disconnected black components dominate the structure of the image yielding a negative Euler characteristic in accordance with the function $\chi$ shown in Fig. 4(c). This measure indicates a negative mean curvature counting curvatures at boundaries negative, if the boundary curve is bended towards the black region as described above. On the other end at high thresholds one observes in Fig. 2(c) an inverted image with many disconnected white components, thus a positive mean curvature, and therefore a positive Euler characteristic. In between, at intermediate thresholds $\rho$ highly connected and intertwined black and white stripes occur, where the mean curvature is almost zero and the number of black and white components is balanced. The area $v$, the boundary length $s$, and the Euler characteristic $\chi$ are called the Minkowski measures for two-dimensional patterns.

## III. RESULTS FOR TURING PATTERNS

In order to apply the Minkowski measures to Turing patterns generated by a diffusion-reaction system we calculate for each threshold $\rho$ and each pattern reported in Ref. [1] the white area $v$, the length $s$ of the boundaries, and the integral of the curvature along the boundaries, i.e., the Euler characteristic $\chi$. Especially we analyzed each pattern indicated by the ''phase-diagram'' in Fig. 10 of Ref. [1] to study transitions of patterns.

Surprisingly, it turns out that there are simple combinations of the quantities $v(\rho)$, $s(\rho)$, and $\chi(\rho)$, namely,

$$p_v(\rho)=\tanh^{-1}(2v-1),$$

$$p_s(\rho)=\frac{s}{v(1-v)}=4s\,\cosh^2[p_v(\rho)], \tag{1}$$

and

$$p_\chi(\rho)=\frac{\chi}{s},$$

such that the experimental data (considered as functions of the threshold $\rho$, which is normalized to the interval $[-1,1]$ for convenience) may be describe quite well by polynomials of very low degree, i.e.,

$$p_v(\rho)\approx p_v^{(0)}+p_v^{(1)}\rho+p_v^{(2)}\rho^2+p_v^{(3)}\rho^3,$$

$$p_s(\rho)\approx p_s^{(0)}+p_s^{(1)}\rho+p_s^{(2)}\rho^2+p_s^{(3)}\rho^3+p_s^{(4)}\rho^4, \tag{2}$$

and

$$p_\chi(\rho)\approx p_\chi^{(0)}+p_\chi^{(1)}\rho+p_\chi^{(2)}\rho^2+p_\chi^{(3)}\rho^3,$$

which approximate the functions $p_v(\rho)$, $p_v(\rho)$, and $p_v(\rho)$ very accurate. This holds for all the patterns reported in Ref. [1]. That is, these spatial combinations of $v$, $s$, and $\chi$ may be described by a few parameters for different patterns and are thus in this sense universal in character.

In Fig. 5 we show for the same patterns used for Fig. 4, i.e., for a hexagonal state (full lines), a lamellar stripe structure (dashed), and a turbulent pattern (dashed-dotted), the three quantities (a) $p_v(\rho)$, (b) $p_s(\rho)$, and (c) $p_\chi(\rho)$ as functions of the threshold $\rho$. The thin full line in Fig. 5 is the best fit to the functions, which can hardly be distinguished from the experimental data.

The coefficients for the polynomials shown in Fig. 5 are given in Table I to illustrate typical values. It was not possible to fit the data curves with polynomials of lower orders than the one used in the ansatz. Higher orders were not necessary to improve the accuracy. The coefficients $p_\mu^{(i)}$ $(i=1,\ldots,4,\ \mu=v,s,\chi)$ depend on the control parameters as, for instance, the concentration of malonic acid or the temperature, but they are reproducible by unchanged experimental conditions. Moreover, the fits are not only satisfying with sufficient accuracy at intermediate thresholds near zero but also at the very ends, where only few isolated components remain in the images.

Whereas the functions seems to be symmetric in the threshold $\rho$ for stripe and turbulent patterns, the functions display a dominance of black regions for hexagonal patterns. The symmetry observed in Fig. 5 is reflected by the coefficients $p_v^{(0)}$, $p_v^{(2)}$, $p_s^{(1)}$, $p_s^{(3)}$, $p_\chi^{(0)}$, and $p_\chi^{(0)}$, which are for stripes and turbulent patterns, but not for the hexagons, at least a magnitude smaller than the dominant terms.

Nevertheless for the hexagon patterns the values of the functions at the very ends, at $\rho=1$ and $\rho=-1$, show the same symmetric relations, i.e., $p_v(-1)\approx -p_v(1)$, $p_s(-1)\approx p_s(1)$, and $p_\chi(-1)\approx -p_\chi(1)$. Thus the coefficients of the polynomials obey approximately $p_v^{(0)}\approx -p_v^{(2)}$, $p_s^{(1)}\approx -p_s^{(3)}$, and $p_\chi^{(0)}\approx -p_\chi^{(2)}$, as one can see in Table I. Moreover, we found that the value $p_v(-1)=-p_v(1)\approx 2.5$ is not influenced by control parameters like the malonic acid concentration (see Fig. 5).

The first result of this integral geometric method for pattern analysis is that the area $v$ of the white domains as a function of the threshold $\rho$ is given mainly by a hyperbolic tangent profile and that the boundary length $s$ is proportional to the product $v(1-v)$, i.e., to the product of the areas of black and white components, respectively. The particular functional forms in Eq. (1) are chosen because of the occurrence of these functions in many fields of physics. But the connection to the reaction-diffusion system considered here is not clear and needs to be investigated. Although we find these functional forms for all of the chemical patterns reported in Ref. [1], we could not see them in patterns generated by other chemical reactions or by computer simulation.

The second, even more important result is that the dependence on the experimental conditions like the concentration of malonic acid is reflected only in a finite number of coefficients $p_\mu^{(i)}$. The functional form of the measures $v$, $s$, and $\chi$ remains the same, i.e., it is given always by polynomials of low order.

The third and most striking result can be seen when the dependence of the coefficients on the control parameters is considered. We show, for instance, in Fig. 6 for seven different concentrations $[H_2SO_4]_0^B$ (mM) at constant $[ClO_2^-]_0^A=20$ mM the experimental curve $p_\chi(\rho)$ and its best fit using a cubic polynomial. The other control parameters were fixed at the values given for Fig. 10 of Ref. [1]. The shape of the polynomial $p_\chi(\rho)$ indicates a transition from hexagonal point patterns (full lines at $[H_2SO_4]_0^B=17$, 28, 45, and 100 (mM)) to turbulent structures (dash-dotted lines at $[H_2SO_4]_0^B=2$, 5, 10 (mM)). For all turbulent patterns the polynomial is nearly a straight line with no constant, quadratic, or cubic term and shows therefore a zero at $\rho=0$. In contrast, for the hexagons these terms cannot be neglected. Especially the quadratic term yields an asymmetry in the functional form of the threshold $\rho$. The similarity to the symmetry breaking mechanism at thermodynamic phase transitions is obvious, although the physical connection is not made yet. The transition seems to be continuous with steadily decreasing cubic and quadratic terms in the polynomial. They remain almost zero for the turbulent patterns despite the change of the control parameters. The inset shows the coefficient $p_\chi^{(0)}$ of the polynomial $p_\chi(\rho)$, i.e., its value at $\rho=0$, as a function of the concentration $[H_2SO_4]_0^B$ (mM). At each concentration six different patterns were analyzed. This measure reflects the asymmetry in the threshold $\rho$ of the polynomials and is therefore almost zero as long as the pattern is turbulent and it increases when hexagonal structures

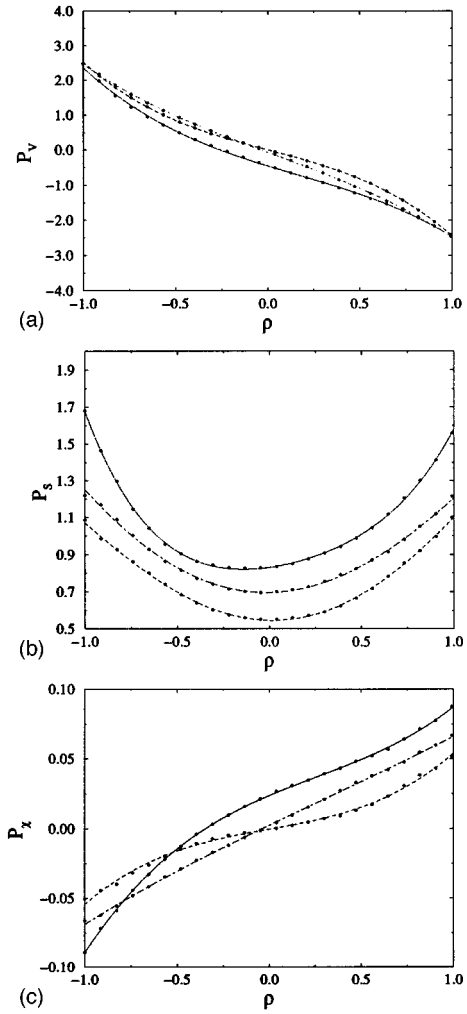


FIG. 5. The same patterns as in Fig. 4, a hexagonal state (full lines), a lamellar stripe structure (dashed), and a turbulent pattern (dash-dotted), are used to illustrate the functional form of the Minkowski measures, i.e., of (a) the area fraction $p_v(\rho)=\tanh^{-1}(2v-1)$, (b) the boundary length $p_s(\rho)=s/v(1-v)$, and (c) the Euler characteristic $p_\chi(\rho)=\chi/s$. The lines are best fits to the experimental data (black dots) using cubic and fourth-degree polynomials. The accuracy is remarkable and could not be achieved with polynomials of lower orders. The asymmetry of the measures for the hexagonal pattern, which can be seen in Fig. 4, are reflected by quadratic terms in the polynomials.

TABLE I. Typical values for the coefficients $p_\mu^{(\nu)}$ of the polynomials $p_\mu(\rho)$ for hexagonal, stripe, and turbulent patterns. Coefficients which are at least a magnitude smaller than the dominant terms are set in parentheses to illustrate the apparent symmetry of the polynomials.

| Pattern type $\mu$ | $p_\mu^{(0)}$ | $p_\mu^{(1)}$ | $p_\mu^{(2)}$ | $p_\mu^{(3)}$ | $p_\mu^{(4)}$ |
|---|---|---|---|---|---|
| Hexagons, $v$ | $-0.45$ | $-1.59$ | 0.397 | $-0.82$ | |
| Hexagons, $s$ | 0.83 | 0.14 | 0.43 | $-0.18$ | 0.36 |
| Hexagons, $\chi$ | 0.024 | 0.056 | $-0.025$ | 0.033 | |
| Stripes, $v$ | (0.0096) | $-1.39$ | (0.030) | $-1.09$ | |
| Stripes, $s$ | 0.55 | $(-0.021)$ | 0.599 | (0.035) | $(-0.062)$ |
| Stripes, $\chi$ | $(-0.00020)$ | 0.024 | $(-0.000013)$ | 0.031 | |
| Turbulent, $v$ | $(-0.063)$ | $-1.93$ | (0.058) | $-0.536$ | |
| Turbulent, $s$ | 0.697 | (0.019) | 0.554 | $(-0.4)$ | $(-0.023)$ |
| Turbulent, $\chi$ | (0.0026) | 0.063 | $(-0.0039)$ | (0.0044) | |

emerge. We find a pattern transition from turbulent stripes to hexagons at a concentration of 17 mM compared with 45 mM indicated by the phase diagram in Fig. 10 of Ref. [1].

In Fig. 7 we show for five different concentrations of malonic acid $[CH_2(COOH)_2]_0^B$ (mM) the experimental curve $p_\chi(\rho)$ and its best fit using a cubic polynomial. The other control parameters were held fixed at the values given for Fig. 7 of Ref. [1]. The shape of the polynomial $p_\chi(\rho)$ reflects clearly the transition from stripe patterns (full lines at $[CH_2(COOH)_2]_0^B = 11,12$ (mM)) to turbulent structures (dash-dotted lines at $[CH_2(COOH)_2]_0^B = 8,9,10$ (mM)). For all turbulent patterns the polynomial is nearly a straight line, in particular without cubic term. But for the stripes the cubic cooefficient is not small compared to the linear term. In contrast to the hexagons, where the quadratic term dominates the shape of the curve, it remains zero for stripe patterns analyzed here.

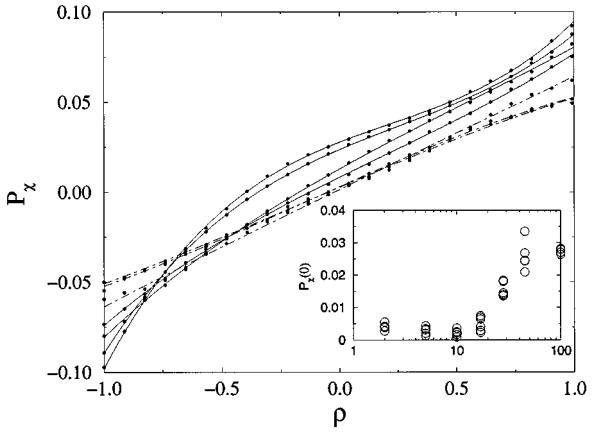


FIG. 6. The polynomial $p_\chi(\rho)$ indicates a transition from hexagonal point patterns (full lines) to turbulent structures (dash-dotted) as a function of $[H_2SO_4]_0^B$ (mM) at constant $[ClO_2^-]_0^A = 20$ mM. The other control parameters were held fixed at the values given for Fig. 10 of Ref. [1]. The transition seems to be continuous with decreasing cubic and quadratic terms in the polynomial. They remain zero for the turbulent patterns. As in Fig. 5, the lines are best fits to the experimental data (black dots). The inset shows the coefficient $p_\chi^{(0)}$ of the polynomial $p_\chi(\rho)$, i.e., its value at $\rho = 0$, as a function of the concentration $[H_2SO_4]_0^B$ (mM). We find a pattern transition from turbulent stripes to hexagons at a concentration of 17 mM compared with 45 mM indicated by the phase diagram in Fig. 10 of Ref. [1].

The insets show the coefficients $p_\chi^{(1)}$ and $p_\chi^{(3)}$, respectively, as a function of the malonic acid concentration $[CH_2(COOH)_2]_0^B$ (mM). Again at each concentration six different patterns were analyzed. The deviation of the values at 12 mM from the ones at 11 mM might result from an insufficient relaxation time for the pattern to relax into its final state [25]. However, we observe a symmetry breaking in the polynomial when the type of pattern changes. The discontinuous pattern transition with a sharp jump from a turbulent state to stripes occurs at a concentration of 10 mM in agreement with the quantities shown in Fig. 8 of Ref. [1].

## IV. CONCLUSION

Relating to our three main findings we want to focus on three questions.

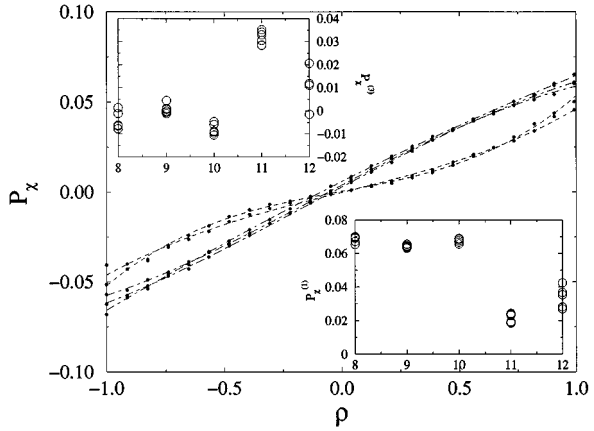


FIG. 7. The transition from stripe patterns (dashed) to turbulent structures (dash-dotted) exhibits a jump in the cubic term in the polynomial $p_\chi(\rho)$ as a function of malonic acid concentration $[CH_2(COOH)_2]_0^B$. The other control parameters were held fixed at the values given for Fig. 7 in Ref. [1]. As in Fig. 5 the lines are best fits to the experimental data (black dots). The insets show the coefficients $p_\chi^{(3)}$ and $p_\chi^{(1)}$, respectively, as a function of malonic acid concentration $[CH_2(COOH)_2]_0^B$. As in Fig. 6, the cubic term is zero for the patterns in the turbulent phase but nonzero for the stripes. In contrast to the hexagon patterns the quadratic term remains small.

(1) Why is the white area essentially a hyperbolic tangent profile in the threshold $\rho$? Despite the occurrence of this profile in such diverse fields as thermal statistics of a paramagnet, the width of an fluid interface, or the mean field solution of a $\phi^4$-field theory, the connection to the reaction-diffusion system is not clear yet.

(2) Why are the measures $p_v(\rho)$, $p_s(\rho)$, and $p_\chi(\rho)$ finite order polynomials in the threshold $\rho$? They do not need to be that. However, in many models for statistical geometries like the Boolean grain model, similar polynomial behaviors of the Minkowski functional do occur [24]. But what is the underlying statistical model in this case, if there is one?

(3) Why is there a symmetry breaking in the mean curvature, i.e., in the Euler characteristic as a measure for the topology of patterns? Is it possible to formulate a mesoscopic theory of pattern transitions in analogy to the Landau theory for thermodynamic phase transitions?

The primary conclusion is that Minkowski measures, in particular the Euler characteristic, describe quantitatively irregular spatial patterns and their transitions in a morphological way and might be capable to classify pattern transitions in a similar way like thermodynamic phase transitions.

## ACKNOWLEDGMENTS

It is a pleasure to thank H. Swinney and Q. Ouyang for providing the data and the friendly support at the Center for Nonlinear Dynamics. I would also like to acknowledge fruitful discussions with M. Marder. This work was financially supported by the Deutsche Forschungsgemeinschaft (DFG).

[1] Q. Ouyang and H. L. Swinney, Chaos **1**, 411 (1991).
[2] Q. Ouyang and H. L. Swinney, Nature **352**, 610 (1991).
[3] V. Castets, E. Dulos, J. Boissonade, and P. De Kepper, Phys. Rev. Lett. **64**, 2953 (1990).
[4] P. De Kepper, V. Castets, E. Dulos, and J. Boissonade, Physica D **49**, 161 (1991).
[5] J. Boissonade, V. Castets, E. Dulos, and P. De Kepper, in *Bifurcation and Chaos: Analysis, Algorithms, Applications*, edited by T. Küpper, F. W. Schneider, R. Seydel, and H. Troyer, International Series of Numerical Mathematics Vol. 97 (Birkhäuser, Basel, 1991), p. 67.
[6] J. Maselko and K. Showalter, Physica D **49**, 21 (1991).
[7] A. Pocheau, V. Croquette, and P. Le Gal, Phys. Rev. Lett. **55**, 1094 (1985).
[8] V. Steinberg, E. Moses, and J. Fineberg, Nucl. Phys. B (Proc. Suppl.) **2**, 109 (1987).
[9] R. Ribotta and A. Joets, in *Cellular Structures and Instabilities*, edited by J. E. Wesfried and S. Zaleski (Berlin, Springer, 1984).
[10] N. B. Tufillaro, R. Ramshankar, and J. P. Gollub, Phys. Rev. Lett. **62**, 422 (1989).
[11] J. P. Gollub and R. Ramshankar, in *New Perspectives in Turbulence*, edited by S. Orszag and L. Sirovich (Springer, Berlin, 1990).
[12] P. Coullet, L. Gil, and J. Lega, Phys. Rev. Lett. **62**, 1619 (1989).
[13] J.-P. Eckmann and I. Procaccia, Phys. Rev. Lett. **66**, 891 (1991).
[14] G. H. Gunaratne, Q. Ouyang, and H. L. Swinney, Phys. Rev. E **50**, 2802 (1994); G. H. Gunaratne, R. E. Jones, Q. Ouyang, and H. L. Swinney, Phys. Rev. Lett. **75**, 3281 (1995).
[15] T. Passot and A. C. Newell, Physica D **74**, 301 (1994).
[16] A. Rosenfeld and A. C. Kak, *Digital Picture Processing* (Academic, New York, 1976).
[17] L. A. Santaló, *Integral Geometry and Geometric Probability* (Addison-Wesley, Reading, MA, 1976).
[18] J. Serra, *Image Analysis and Mathematical Morphology* (Academic, New York, 1982), Vols. 1 and 2.
[19] A. M. Turing, Philos. Trans. R. Soc. London Ser. B **327**, 37 (1952).
[20] Overviews can be found in G. Nicolis and I. Prigogine, *Self-organization in Nonequilibrium Chemical Systems* (Wiley, New York, 1977); H. Haken, *Synergetics, an Introduction* (Springer, Berlin, 1977); Y. Kuramoto, *Chemical Oscillations, Waves, and Turbulence* (Springer, Berlin, 1984); R. J. Field and M. Burger, *Oscillations and Traveling Waves in Chemical Systems* (Wiley, New York, 1985); H. Meinhardt, *Models of Biological Pattern Formation* (Academic, New York, 1986); A. Babloyantz, *Molecules, Dynamics and Life* (Wiley, New York, 1986); J. D. Murray, *Mathematical Biology* (Springer, New York, 1989); R. Kapral and K. Showalter, *Chemical Waves and Patterns* (Kluwer Academic, Dordrecht, 1995).
[21] K. R. Mecke, Ph.D. thesis, Munich, 1993.
[22] C. Likos, K. R. Mecke, and H. Wagner, J. Chem. Phys. **102**, 9350 (1995).
[23] K. R. Mecke, Th. Buchert, and H. Wagner, Astron. Astrophys. **288**, 697 (1994).
[24] K. R. Mecke and H. Wagner, J. Stat. Phys. **64**, 843 (1991).
[25] Q. Ouyang (private communication).